Substitution of Re^{7+} into $CaMnO_3$, an efficient free electrons generation dopant for tuning of thermoelectric properties

J. Felix Shin,[a] Hongjun Niu,[a] Jonathan Alaria,[b] John B. Claridge,*[a] and Matthew J. Rosseinsky,*[a]

Highly dense $CaMn_{1-x}Re_xO_3$ ($0 \leq x \leq 0.04$) samples were prepared by solid state synthesis. The effect of Re doping was assessed by the characterisation of crystal structure, oxygen content, electrical and thermal transport properties. The oxidation state of the substituted Re was determined by X-ray absorption near edge spectra to be Re^{7+}, and led to expansion of the lattice and an increase in electron carrier concentration due to the formation of Mn^{3+}. The thermal behaviour of the electrical conductivity and the thermopower over a wide temperature range allowed identification of different conduction mechanisms: (1) below 110 K 3D variable range hopping, (2) between 110 K – 650 K small polaron transport, and (3) above 650 K activation of carriers over a mobility edge. Evaluation of the power factor expected for different dopant oxidation states as a function of dopant concentration shows that the doping strategy using a heavy heptavalent ion allows accessing the peak power factor at lower dopant concentration, lowering the amount of non-ionised impurities and therefore improves the electronic substitution efficiency, the ratio of activated carriers over the nominal doping concentration, compared to previously studied dopants. An increased power factor and reduced lattice thermal conductivity are obtained with a peak figure of merit ZT = 0.16(3) at 947 K for $CaMn_{0.98}Re_{0.02}O_3$. This is an approximately two-fold increase compared to undoped $CaMnO_3$, and is comparable to the highest values reported for highly dense B-site doped $CaMnO_3$.

Introduction

Thermoelectric power generators are solid state devices that directly convert heat energy into electricity and their applications include automotive waste heat recovery, solar/geothermal power conversions and space vehicle power source.[1-5] There are no moving parts involved, thus they are silent, reliable and versatile.[6,7] They are particularly attractive in industrial waste heat recovery since it is estimated that 20 - 50 % of energy consumed in this sector is eventually lost to waste heat, but the materials in such applications require high thermal stability (at ≈ 1000 K), oxidation resistance in air and low toxicity as well as high efficiency.[8-11]

Perovskite type $CaMnO_3$ is one of the n-type thermoelectric oxides that fulfils the majority of the requirements but falls short on the efficiency of conversion,[1,8,9] which is usually assessed by the dimensionless figure of merit $ZT = S^2T/\rho\kappa$, where S is the Seebeck coefficient, ρ the electrical resistivity and κ the thermal conductivity at the temperature T. The common approaches to improve ZT for $CaMnO_3$ are aliovalent substitution at either the A- or B-sites; (i) the substitution of species of differing mass in the $CaMnO_3$ lattice results in the presence of phonon scattering centres, which inhibits the migration of thermal energy as vibrations, thus reduces the lattice thermal conductivity of the system, and (ii) the introduction of higher charged species increases charge carrier concentration by charge compensation (*i.e.* introduction of d^4 Mn^{3+} carriers into the integer valence d^3Mn^{4+} Mott insulator) following the Kröger-Vink notation:

$$(n+1)Mn_{Mn}^{\times} = nMn_{Mn}' + X_{Mn}^{n\bullet} \quad (1)$$

where an element X has the oxidation state of n + 4.

The creation of free electrons in the system results in an increased conductivity and a reduced Seebeck coefficient.[12-27] Thus the best compromise was sought to optimise the effect of the substitution to maximise the power factor defined as S^2/ρ. Recently, Thiel *et al*. reported significant improvements in thermoelectric properties of $CaMnO_3$ through B-site modification with elements that are both heavy and display higher oxidation states such as Nb, Ta where n = 1, W and Mo where n = 2.[28,29] The electrical properties of these electron doped $CaMnO_3$ are often described with the small polaron-hopping-based mechanism and it was shown that higher charged species are more suitable to increase the conductivity. For both n = 1 and n = 2 doping strategies, they observed that above a doping concentration threshold (x = 0.08 and x = 0.04 respectively) the amount of free carriers generated by the impurities is smaller than the nominal dopant concentration and therefore the efficiency of the electronic substitution is decreased,[28,29] which can be due to reduced mobility of the carriers as the scattering by impurities is increased and the generation of non-ionised impurities with localised electrons. A possible solution to this problem is to explore dopants with n > 2 which would reduce the amount of dopant necessary to achieve the same level of electronic substitution.

Re is a third transition series element which exhibits various oxidation states in oxide chemistry; three binary oxides (ReO_2, ReO_3 and Re_2O_7) are known and many ordered double perovskites containing Re^{5+}, Re^{6+} and Re^{7+} can be isolated.[30,31] The possibility of substituting Mn with Re^{7+} in $CaMnO_3$ (corresponding to n = 3) in the compensation mechanism with a single Re^{7+} in place of Mn^{4+} creating three Mn^{3+} could offer an effective alternative doping strategy to overcome the current limitation. In addition, Re offers a large mass difference compared to Mn, thus it is expected to act as an excellent phonon scattering centre. Previous reports of Re-substituted $CaMnO_3$ have focused

on the low temperature electrical properties for colossal magneto-resistance,[32] and the Re oxidation state was not experimentally determined, and was reasonably assumed to be Re^{5+}. This work demonstrates the possibility of tuning the carrier concentration in this system with a resistivity as low as 4.1 mΩ cm and a Seebeck coefficient of -100 μV K^{-1} at 300 K for a 6% Re atomic substitution corresponding to a 300 K power factor of 2.5 μW cm^{-1} K^{-2} which is similar to other doped B site doped $CaMnO_3$ compounds.[14-16,18] In our study we have determined experimentally that the Re oxidation state is 7+ in this system and therefore corresponds to n = 3 which is higher than that of previous dopants. By measuring the electrical and thermal properties over a wide range of temperature (4 K – 947 K), we established the different conduction mechanisms in different temperature regimes. The high temperature (372 K – 947 K) thermoelectric properties show that the incorporation of a heptavalent cation in $CaMnO_3$ is an effective strategy to improve the power factor in this system.

Experimental

High purity (≥ 99.9%) $CaCO_3$, MnO_2 and Re metal were used to prepare $CaMn_{1-x}Re_xO_3$ ($0 \leq x \leq 0.04$) samples. The powders were ball-milled in 2-propanol with ZrO_2 balls (350 rpm for overnight, Fritsch Pulverisette 7 Planetary Mill), dried and heated initially to 1173 K for 6 hours followed by 1523 K for 12 hours before ball-milling again. The resulting powders were pressed as pellets (1.3 cm diameter) using uniaxial press first and further pressed using cold isostatic press with maximum pressure of 30k psi. The resulting discs were sintered at 1323 – 1623 K for 24 hours which slowly cooled (0.2 K min^{-1}) to 873 K to avoid the disintegration due to the cubic to orthorhombic phase transition,[12] then cooled to room temperature by turning off the furnace. Density of the sintered pellets was calculated with the Archimedes method. The optimised sintering process afforded ceramics with a density > 98% as this is essential for an accurate assessment of the thermoelectric properties.[33] All the samples prepared in this study are crack free as shown in Supplementary Figure S1 and have a relative density of ≥ 98(1)%, almost reaching the theoretical limit as presented in Supplementary Table S1. The critical effect of the density on the electrical properties of an undoped $CaMnO_3$ ceramic is presented in Supplementary Figure S2.

The oxygen content was measured for all samples using thermogravimetric profiles collected with a TA Instruments Q600 SDT on 100 mg of powder samples derived from the sintered pellets. Samples were heated (10 K min^{-1}) to 1223 K under flowing 4 vol. % H_2/N_2. The reduction products were identified by X-ray diffraction (Supplementary Figure S3). Based on the identities of the reduction products, the room temperature oxygen vacancy content was calculated and presented in Table S1. All the samples showed negligible oxygen vacancy content ($\delta \leq 0.01$). The slow cooling process was also used to minimise the amount of oxygen vacancies in the system[12,34,35] which would introduce undesired carriers.

Phase purity was determined initially using laboratory X-ray powder diffraction data (XRD) collected on a Bruker-AXS D8 Advance diffractometer with a fine focus Mo K_α source (λ = 0.71073 Å). Synchrotron XRD data recorded on beamline I11 (λ = 0.825972 Å) at Diamond Light Source, UK allowed precise lattice parameter determination and the identification of impurities with high sensitivity.

Re L_3-edge X-ray absorption near edge spectra (XANES) were collected on Beamline B18 at Diamond Light Source, U.K. Samples were diluted with cellulose powder and pressed into pellets approximately 1 mm thick. Data were collected in transmission mode and spectra were normalized using ATHENA.[36] Reference samples for different Re oxidation states were prepared by a standard solid state method (Supplementary Figure S4): Ba_2YReO_6 for Re^{5+}, Ba_2CaReO_6 for Re^{6+} and Ba_2NaReO_6 for Re^{7+}.

The sintered pellets were cut into a bar shape (≈ 2 x 4 x 8 mm) and the resistivity and the Seebeck coefficient were measured using an ULVAC ZEM3 Seebeck coefficient/electric resistance measuring system with four probe arrangement under He atmosphere from 326 to 947 K. The low temperature electrical and thermal properties were measured using the Thermal Transport Option in a DynaCool system (Quantum Design) under vacuum from 4 to 370 K. Thermal expansion profiles were collected using Netzsch DIL 402C under static air with temperature range between 300 to 973 K. Thermal diffusivity of sintered pellets which were polished and coated with graphite, were measured using

Netzsch LFA 457 under flowing N_2 (100 ml min^{-1}) with temperature range between 323 to 948 K. Heat flux profile of thin slices of sintered pellets were obtained using Netzsch DSC 404 F1 under flowing N_2 (50 ml min^{-1}) with temperature range between 323 to 948 K. Measurement of the reference sapphire (Netzsch) under the same conditions and heating programme was used to calculate the heat capacities of the samples. The error for the resistivity and the Seebeck coefficient is ≈ ±5 % and that of the calculated thermal conductivity is ≈ ±6 %, which are shown in the relevant figures.

Result and discussion

The incorporation of Re^{7+}

The synchrotron XRD patterns for the $CaMn_{1-x}Re_xO_3$ ($0 \leq x \leq 0.04$) samples are presented in Figure 1a. They are all single phase samples adopting orthorhombic symmetry with the *Pnma* space group confirmed by full-profile analysis with the Pawley method, which means that all the Re-doped $CaMnO_3$ are isostructural to the parent $CaMnO_3$. All the peaks showed a gradual shift to lower angle with higher doping level which is highlighted by the most intense Bragg reflections in Figure 1b, thus indicating lattice expansion with increased Re content. The lattice parameters for the samples obtained by Pawley fitting are plotted in Figure 1c and all three axes showed monotonic increase with Re content similar to that observed for pentavalent (Nb^{5+}, Ta^{5+} and Ru^{5+}) and hexavalent (Mo^{6+} and W^{6+}) dopants.[13-16,28] The ionic radii for the each cation on the B-site are Mn^{3+} = 0.645 Å, Mn^{4+} = 0.53 Å and potentially Re^{5+}=0.58 Å, Re^{6+}=0.55 Å or Re^{7+} = 0.53 Å.[37] The presence of Re alone in any of the candidate oxidation states would not be expected to induce any major change in the lattice parameter since its radius is close to that of Mn^{4+}, but the creation of larger Mn^{3+} by the charge compensation mechanism will certainly expand the lattice. To assess the degree of electronic substitution (n = 1, 2 or 3 in Equation 1) and determine the charge carrier mechanism it is crucial to determine the Re oxidation state.

The oxidation state of Re in the $CaMn_{1-x}Re_xO_3$ ($0.005 \leq x \leq 0.04$) samples was determined by XANES. All the Re doped samples have the same Re oxidation state as all the spectra showed the same edge position at 10539.4 eV (Figure 2 inset). This is a higher energy than those of Re^{5+} (10537.8 eV) and Re^{6+} (10538.7 eV) in Ba_2YReO_6 and Ba_2CaReO_6 reference samples respectively, and corresponds to the edge position of Re^{7+} (10539.2 eV) in the Ba_2NaReO_6 reference sample (Figure 2). This was not unexpected as the use of ambient air in the preparation of Ba_2NaReO_6 resembles the synthetic conditions for the $CaMn_{1-x}Re_xO_3$ series more closely than the other two Re^{5+} and Re^{6+} reference samples which were prepared under reduced oxygen partial pressure in sealed tubes.

The rate of expansion of the cell volume as a function of the doping level x for the Re doped samples is 68(2) $Å^3\ x^{-1}$ which is greater than 53(3) $Å^3\ x^{-1}$ for the W doped series, consistent with Re adopting the +7 oxidation state.[12] The greater cell expansion rate by the incorporation of higher charged species was demonstrated by the comparison between penta- and hexavalent dopants and rationalised by the introduction of the increased number of Mn^{3+} per substitution.[28] In conjunction with the cell parameter increase which matches well with the Re oxidation state from the XANES study, it is evident that the incorporation of Re^{7+} into $CaMnO_3$ perovskite structure has been successful.

The electrical and thermoelectric properties: determination of the conduction mechanism

The resistivity and Seebeck coefficient for the $CaMn_{1-x}Re_xO_3$ ($0 \leq x \leq 0.04$) samples as a function of temperature between 326 K and 947 K are shown in Figure 3. The negative values of the Seebeck coefficient for the series indicate dominant n-type conduction expected based on the dopant charge state. The resistivity and the absolute value of the Seebeck coefficient for all the samples increase with increasing temperature in this temperature interval which is typically observed in compounds

where the conduction mechanism is limited by the mobility of the carriers such as metals, degenerate semiconductors and polaronic transport at high temperature. It is widely agreed that Mott's adiabatic small-polaron conduction model can be used for n-type calcium manganites at high temperature.[38] In this case, the resistivity is activated but does not follow the Arrhenius law observed in broad band semiconductors and a pre-exponential factor has to be included. This can be expressed in the form:

$$\rho(T) = \rho_0 T exp\left(\frac{E_\rho}{k_B T}\right)$$

where E_ρ is an activation energy corresponding to half of the polaron binding energy. Since the Seebeck coefficient is governed by thermal activation of carriers across a barrier, it has a similar form to that of a band semiconductor and can be written as:

$$S(T) = \frac{k_B}{e}\left(\frac{E_s}{k_B T} + A\right)$$

where E_s is the activation energy corresponding to the Fermi energy and A is a constant associated with the spin and mixing entropy,[39] which leads in the high temperature limit to the Heikes formula [40] and the Seebeck coefficient converge towards:

$$S_{Heikes}(T \to \infty) = \pm \frac{k_B}{e} \ln\left[g\left(\frac{1-y}{y}\right)\right]$$

where *g* is an electronic degeneracy parameter and y is the carrier concentration.

One of the signatures of small polaronic conduction is the difference of energies involved in the resistivity and Seebeck description. If the transport was dominated by the thermal activation of carriers to a mobility edge, both activation energies would be equal ($E_\rho = E_S$), whereas for small polaron systems $E_\rho > E_S$. Moreover, when E_ρ is similar to $k_B T$, the exponential term become negligible and the temperature dependence of the resistivity would be similar to a metal or degenerate semiconductor. The activation energies extracted for doped $CaMnO_3$ are of the order of 30 meV and it is therefore difficult to distinguish if the electrical properties should be described using band semiconductor or hopping models.[12,24,29,41] To differentiate between these models it is necessary to measure the low temperature electrical and thermal properties of these compounds.

The log(ρ) *vs.* log(*T*) plot for x = 0.03 from 35 to 947 K shown in Figure 4a exhibits a significant decrease in the resistivity from 35 to 200 K, the negative gradient persists up to 300 K then changes sign suggesting an activated behaviour with an activation energy larger than 30 meV up to 300 K and therefore ruling out the degenerate semiconductor possibility.

Figure 4a also allows the identification of different conduction mechanisms in specific temperature regimes. A slope ν = -4.0(1) is obtained between 35 K to 110 K which corresponds to 3D variable range hopping conduction.[42] No temperature region shows a slope ν = -1 which would correspond to an activated broad band semiconductor following a conventional Arrhenius law. This suggests a thermal dependence of the pre-exponential factor as described above for the small polaron model. The logarithmic plot of ρ/T *vs.* 1/*T* in the temperature range 110 K – 900 K is presented in Figure 4b and two linear regions can be identified: (i) 110 K – 200 K with an activation energy $E_{\rho 1}$ = 40.0(2) meV

and (ii) 250 K – 950 K with an activation energy $E_{\rho 2}$ = 25.4(1) meV. To determine whether the small polaron model is valid in the complete temperature range studied, these activation energies have to be compared with the activation energies extracted from the temperature dependence of the Seebeck coefficient. Figure 4c presents the temperature dependence of the Seebeck coefficient as a function of 1/*T* between 200 K – 1000 K for x = 0.03 with two linear region identified: (i) between 200 K – 650 K with an activation energy E_{s1} = 15(1) meV and (ii) between 650 K – 1000 K with an activation energy E_{s2} = 45(2) meV. Previous reports discussing the conduction mechanism in B-site doped $CaMnO_3$ based on high temperature measurement have concluded that the conduction occurs via activation to the mobility edge,[12] since they find a near-zero polaron-transport activation energy defined as ½W = E_ρ - E_S whereas in A-site substituted $CaMnO_3$ it was observed that $E_\rho > E_S$,[22] which is characteristic of electron transport due to polarons.[43] In our case we observe a transition from (i) transport occurring via thermally activated hopping of small polarons between 110 K – 650 K (Fig 4b and 4c blue line) to (ii) transport occurring via activation of carriers to a mobility edge for T > 650 K (Fig 4b and 4c red line) where the small polaron model is not valid to describe the electrical and thermoelectric properties.

Power Factor analysis

The first step to design efficient thermoelectric materials is to obtain large power factors, which is conventionally done by optimising the doping concentration. The power factors for $CaMn_{1-x}Re_xO_3$ (0 ≤ x ≤ 0.04) as a function of temperature are shown in Figure 5a, revealing a minor temperature dependence. By combining the equations for the Seebeck coefficient and the resistivity in the high temperature limits (> 650 K in our study) the power factor as a function of doping can be computed using the model of Thiel et al.,[29] and can be approximated as:

$$\left(\frac{S^2}{\rho}\right)_T \propto \ln^2\left(\frac{N_A}{c}\right) \cdot N_A \cdot c \qquad (2)$$

where N_A = 1 – (n + 1)x is the number of available hopping sites for itinerant charge carriers (number of Mn^{4+} ions) and c = nx/(1 – x) is the charge-carrier concentration and n = 1 for pentavalent substitution, n = 2 for hexavalent substitution and n = 3 for heptavalent substitution. The advantage of using n = 3 compared to the two previously studied possibilities is illustrated in Figure 5b (solid line) where the maximum power factor for n = 3 is achieved for a smaller substitution concentration. The isothermal power factor measured at 659 K as function of Re content is superimposed with the model described above in Figure 5b (scatter). We obtain a good agreement between the model and the measured power factor with a peak power factor achieved at lower substitution levels compared to penta- and hexavalent dopants which highlights the effectiveness of the n = 3 doping strategy by limiting the reduction in electronic doping at high substitution level observed in previous studies for n = 1 and 2.[29] The x = 0.01 and 0.02 samples exhibited the power factor value of ≈ 4.5 µW cm^{-1} K^{-2} at from 326 to 947 K which is similar to the highest power factor achieved for $CaMn_{0.96}Ta_{0.04}O_3$ which shows a peak value of ≈ 5 µW cm^{-1} K^{-2} at ≈ 350 K.[29]

Thermal conductivity

The experimentally obtained total thermal conductivity and estimated electronic and lattice thermal conductivity for the $CaMn_{1-x}Re_xO_3$ (0 ≤ x ≤ 0.04) samples as a function of temperature is shown in Figure 6. The total thermal conductivity in these solids (κ_{total}) is the sum of two contributions, the

lattice ($\kappa_{lattice}$) arising from energy transferred via phonons and electrical thermal conductivity (κ_{el}) arising from the energy transferred via charge carriers : $\kappa_{el} + \kappa_{lattice} = \kappa_{total}$. In broad band semiconductor and metallic systems the electrical thermal conductivity is commonly approximated with the Wiedemann-Franz law,[44]

$$\kappa_{el} = LT/\rho \quad (3)$$

where *L* is the Lorenz number and for metallic system takes the Sommerfeld value of 2.45 x 10^{-8} W Ω K^{-2}.[45]

If the Wiedemann-Franz law is generally applicable to solids where the charge carriers can be described using a broad band conduction model, it has been shown that in compounds showing strong electron-phonon correlation such as polaronic conductors,[46] perovskite manganites,[47] and cuprate superconductors,[48] the Wiedmann-Franz law is not applicable. In the particular case of small polarons, the transfer of heat is carried with the hopping of a charge carrier and some additional vibrational energy bound to the carrier leading to an electronic thermal conductivity smaller than that of a free carrier.[46] The compounds studied here show a transition from small polaron conduction (between 110 K – 650 K for x = 0.03) to carriers activated over a mobility edge (at T > 650 K for x = 0.03). In the small polaron conduction regime, κ_{el} is expected to be much smaller than the one determined using the free electron Wiedmann-Franz law, whereas in the activated conduction regime the carriers move itinerantly and the free electron Wiedmann-Franz law is valid.

Since the Wiedmann-Franz law for free electron provides an upper limit of κ_{el} regardless of the charge carrier conduction mechanism, the lattice contribution was calculated by subtracting the electronic thermal conductivity estimated using the free electron Wiedmann-Franz law (≤ 0.4 W m^{-1} K^{-1} for the Re doped $CaMnO_3$ series) from the experimentally obtained total thermal conductivity. It is worth noting that the estimated electronic conductivity is smaller than the experimental error of κ_{total} and the use of this approximation, which does not take into account the electron-phonon coupling, in this case is not expected to substantively affect the estimate of the electronic contribution to the total thermal conductivity.

The lattice thermal conductivity decreases with increasing Re content, corresponding to the disruption of phonon migration by the incorporation of the heavy Re atoms in the lattice which acts as point scattering centres. The total thermal conductivity shows the same trend which indicates the majority of the thermal conduction for the series is through the lattice vibration: the electronic contribution is ≈ 2 % for the undoped $CaMnO_3$ and from 12 to 25 % for the x = 0.04 material corresponding to the improved electrical resistivity and decreased lattice thermal conductivity with increasing Re content. The lattice thermal conductivity decreases with increasing temperature which indicates that the disruption of phonon migration is also dominated by phonon-phonon Umklapp scattering.[49]

ZT

ZT for the $CaMn_{1-x}Re_xO_3$ ($0 \le x \le 0.04$) materials increases with increasing temperature (Figure 7a) . Since the *PF* showed no significant temperature dependence, the temperature dependence of *ZT* originates from the thermal conductivity. The variation of *ZT* with Re content at three temperatures (373, 659 and 947 K) is presented in Figure 7b and shows the near-parabolic relation between *ZT* and

Re content, similar to that of the *PF*. The peak is at x = 0.02 with the highest *ZT* value of 0.16(3) at 947 K. There was a shift to higher doping level compared to the *PF* due to the influence of reduced thermal conductivity with increasing Re content. This peak value and the area under the plot of *ZT vs*. *T* are comparable to those of $CaMn_{0.96}Ta_{0.04}O_3$ which is the best highly dense (*i.e.,* where the reported relative density is greater than 90%) B-site doped $CaMnO_3$ so far reported. Not only the *ZT* but also the *PF* and the thermal conductivity of x = 0.02 are comparable to those of $CaMn_{0.96}Ta_{0.04}O_3$, despite the fact that x = 0.02 contains the half of the dopant content compared to $CaMn_{0.96}Ta_{0.04}O_3$. Since Ta and Re have negligible mass difference, this could originate from the increased amount of Mn^{3+} in the Re substitution case. Indeed, Ta/Nb and Mo/W doped samples show similar thermal conductivity as a function of the number of introduced Mn^{3+}. Therefore, it is not only the point defects which decrease the thermal conductivity but also the changes induced by the introduction of the Mn^{3+} such as lattice distortion because of the ionic radii difference.

Conclusions

In summary, we have prepared single phase samples of the $CaMn_{1-x}Re_xO_3$ ($0 \leq x \leq 0.04$) series with orthorhombic *Pnma* symmetry through solid state synthesis. Highly dense samples were obtained by the optimisation of the preparation procedure which is a pre-requisite to assess appropriately the electrical and thermal properties. We have demonstrated using XANES that the substituted Re adopts the +7 oxidation states. Several studies have reported the high temperature thermoelectric properties of $CaMnO_3$ substituted with penta- and hexavalent on the B site but the effect of the incorporation of a heptavalent B cation has not been studied so far. By measuring the electrical and thermoelectric properties in a wide temperature range, we were able to distinguish the different conduction mechanisms dominating in different temperature regimes. Below 110 K a 3D variable range hopping mechanism is observed, followed by small polaron conduction between 110 K - 650 K. At higher temperature, the conduction mechanism is dominated by the activation of carriers above a mobility edge which is similar to band conduction. The detailed understanding of the conduction mechanisms allowed for the analysis of power factor data using a reasonable model for the transport and its comparison with different dopant oxidation states highlighted the beneficial effect of the proposed doping strategy with a significant increase in power factor values compared to that of undoped $CaMnO_3$, where the loss in the magnitude of the Seebeck coefficient was outweighed by the improvement in the resistivity. Moreover it shows that heptavalent substitution generates a peak power factor at lower substitution concentration and therefore avoids the electronic substitution effectiveness reduction observed for penta- and hexavalent substitution. We observe a peak power factor of 4.5(7) $\mu W\ cm^{-1}\ K^{-2}$ for x = 0.02 which is equivalent to the peak power factor reported for Ta^{5+} for x = 0.04. A further positive effect of Re incorporation was the significantly reduced lattice thermal conductivity with relatively small amount of doping compared to penta- and hexavalent dopants; we observe 2.6(2) $W\ \Omega\ K^{-2}$ at 947K for x = 0.02 which required x = 0.04 for the pentavalent dopant Ta. This indicates that Re^{7+} functions as an efficient phonon scattering centre. The maximum *ZT* value of 0.16(3) at 947 K for $CaMn_{0.98}Re_{0.02}O_3$ was obtained, which is two-fold increased from 0.085(10) of undoped $CaMnO_3$ and comparable to 0.15(3) of similarly heavy and highly charged B-site doped $CaMnO_3$, $CaMn_{0.96}Ta_{0.04}O_3$. Overall, the results prove the effectiveness of heavy and heptavalent Re incorporation in improving the thermoelectric properties of $CaMnO_3$.

Acknowledgements

We thank EPSRC for support under EP/N004884. Synchrotron X-ray diffraction work was carried out with the support of Diamond Light Source, UK. XANES experiments were performed under SP14239 as part of the Energy Materials BAG at the Diamond Light Source, UK on beam line B18. We thank C. Tang, C. Murray and S. Day for assistance on Beamline I11 (Diamond Light Source). We thank A. Chadwick, D. Pickup, S. Ramos, G. Cibin, and N. Tapia-Ruiz for assistance on Beamline B18 (Diamond Light Source). M.J.R. is a Royal Society Research Professor.

Footnotes

[a] Department of Chemistry, University of Liverpool, Liverpool L69 7ZD, UK. E-mail: m.j.rosseinsky@liv.ac.uk; j.b.claridge@liv.ac.uk; Fax: +44 (0)1517943589; Tel: +44 (0)1517942297

[b] Department of Physics, University of Liverpool, Liverpool L69 7ZE, UK

References

1. S. Hébert, D. Berthebaud, R. Daou, Y. Breard, D. Pelloquin, E. Guilmeau, F. Gascoin, O. Lebedev and A. Maignan, *J. Phys. Condens. Matter*, 2016, **28**, 13001.
2. J. P. Heremans, *Nature*, 2014, **508**, 327-328.
3. S. Walia, S. Balendhran, H. Nili, S. Zhuiykov, G. Rosengarten, Q. H. Wang, M. Bhaskaran, S. Sriram, M. S. Strano and K. Kalantar-zadeh, *Prog. Mater. Sci.*, 2013, **58**, 1443-1489.
4. J. Karni, *Nat Mater*, 2011, **10**, 481-482.
5. L. E. Bell, *Science*, 2008, **321**, 1457-1461.
6. S. LeBlanc, S. K. Yee, M. L. Scullin, C. Dames and K. E. Goodson, *Renew. Sust. Energ. Rev.*, 2014, **32**, 313-327.
7. M. Zebarjadi, K. Esfarjani, M. S. Dresselhaus, Z. F. Ren and G. Chen, *Energy Environ. Sci.*, 2012, **5**, 5147-5162.
8. J. W. Fergus, *J. Eur. Ceram. Soc.,* 2012, **32**, 525-540.
9. K. Koumoto, R. Funahashi, E. Guilmeau, Y. Miyazaki, A. Weidenkaff, Y. Wang and C. Wan, *J. Am. Ceram. Soc.*, 2013, **96**, 1-23.
10. J. Fleurial, *JOM*, 2009, **61**, 79-85.
11. BCS, Incorporated, 2008, http://www1.eere.energy.gov/manufacturing/intensiveprocesses/pdfs/waste_heat_recovery.pdf, (accessed September 2016)
12. P. Thiel, J. Eilertsen, S. Populoh, G. Saucke, M. Doebeli, A. Shkabko, L. Sagarna, L. Karvonen and A. Weidenkaff, *J. Appl. Phys.*, 2013, **114**, 243707.
13. A. Maignan, C. Martin, C. Autret, M. Hervieu, B. Raveau and J. Hejtmanek, *J. Mater. Chem.*, 2002, **12**, 1806-1811.
14. L. Bocher, M. H. Aguirre, R. Robert, D. Logvinovich, S. Bakardjieva, J. Hejtmanek and A. Weidenkaff, *Acta Materialia*, 2009, **57**, 5667-5680.
15. Y. Q. Zhou, I. Matsubara, R. Funahashi, G. J. Xu and M. Shikano, *Mater. Res. Bull.*, 2003, **38**, 341-346.
16. L. Pi, S. Hébert, C. Martin, A. Maignan and B. Raveau, *Phys. Rev. B*, 2003, **67**, 024430.
17. J. Lan, Y. Lin, H. Fang, A. Mei, C. Nan, Y. Liu, S. Xu and M. Peters, *J. Am. Ceram. Soc.*, 2010, **93**, 2121-2124.

18. R. Kabir, T. Zhang, D. Wang, R. Donelson, R. Tian, T. T. Tan and S. Li, *J. Mater. Sci.*, 2014, **49**, 7522-7528.
19. G. J. Xu, R. Funahashi, Q. R. Pu, B. Liu, R. H. Tao, G. S. Wang and Z. J. Ding, *Solid State Ionics*, 2004, **171**, 147-151.
20. D. Flahaut, T. Mihara, R. Funahashi, N. Nabeshima, K. Lee, H. Ohta and K. Koumoto, *J. Appl. Phys.*, 2006, **100**, 084911.
21. C. Liu, A. Bhaskar and J. J. Yuan, *Appl. Phys. Lett.*, 2011, **98**, 214101.
22. Y. Wang, Y. Sui, X. Wang and W. Su, *Journal of Physics D-Applied Physics*, 2009, **42**. 055010
23. F. P. Zhang, Q. M. Lu, X. Zhang and J. X. Zhang, *Physica Scripta*, 2013, **88**, 035705.
24. Y. Zhu, C. Wang, W. Su, J. Liu, J. Li, Y. Du, X. Zhang, Y. Qin and L. Mei, *J. Electron. Mater.*, 2015, **44**, 414-419.
25. Y. Zhu, W. Su, J. Liu, Y.-C. Zhou, J. Li, X. Zhang, Y. Du and C. Wang, *Ceram. Int.*, 2015, **41**, 1535-1539.
26. L. Bocher, M. H. Aguirre, R. Robert, D. Logvinovich, A. Shkabko, R. Robert, M. Trottmann and A. Weidenkaff, *Iorg. Chem.*, 2008, **47**, 8077-8085.
27. L. T. Hung, N. V. Nong, L. Han, D. L. Minh, K. A. Borup, B. B. Iversen, N. Pryds and S. Linderoth, *J. Mater. Sci.*, 2013, **48**, 2817-2822.
28. P. Thiel, S. Populoh, S. Yoon and A. Weidenkaff, *J. Solid State Chem.,* 2015, **229**, 62-67.
29. P. Thiel, S. Populoh, S. Yoon, G. Saucke, K. Rubenis and A. Weidenkaff, *J. Phys. Chem. C*, 2015, **119**, 21860-21867.
30. A. W. Sleight, J. Longo and R. Ward, *Inorg. Chem.*, 1962, **1**, 245-250.
31. Y. Sasaki, Y. Doi and Y. Hinatsu, *J. Mater. Chem.,* 2002, **12**, 2361-2366.
32. B. Raveau, A. Maignan, C. Martin and M. Hervieu, *Mater. Res. Bull.*, 2000, **35**, 1579-1585.
33. K. A. Borup, J. de Boor, H. Wang, F. Drymiotis, F. Gascoin, X. Shi, L. Chen, M. I. Fedorov, E. Muller, B. B. Iversen and G. J. Snyder, *Energy Environ. Sci.*, 2015, **8**, 423-435.
34. K. Świerczek, B. Dabrowski, L. Suescun and S. Kolesnik, *J. Solid State Chem.*, 2009, **182**, 280-288.
35. M. H. R. Lankhorst and J. E. tenElshof, *J. Solid State Chem.*, 1997, **130**, 302-310.
36. B. Ravel and M. Newville, *J. Synchrot. Radiat.*, 2005, **12**, 537-541.
37. R. D. Shannon and C. T. Prewitt, *Acta Crystallogr., Sect. B: Struct. Crystallogr. Cryst. Chem.,* 1969, **B 25**, 925-946
38. R. Singh, J. Mod. Phys., 2013, **4**, 191-199.
39. M. Jaime, M. B. Salamon, M. Rubinstein, R. E. Treece, J. S. Horwitz and D. B. Chrisey, *Phys. Rev. B*, 1996, **54**, 11914-11917.
40. P. M. Chaikin and G. Beni, *Phys. Rev. B*, 1976, **13**, 647-651.
41. Y. Zhu, C. Wang, W. Su, J. Liu, J. Li, X. Zhang and L. Mei, *J. Solid State Chem.,* 2015, **225**, 105-109.
42. N. F. Mott, *J. Non-Cryst. Solids*, 1968, **1**, 1-17.
43. N. F. Mott and E. A. Davis, *Electronic Processes in Non-Crystalline Materials*, Oxford University Press, Oxford, 1971.
44. R. Franz and G. Wiedemann, *Ann. Phys.*, 1853, **165**, 497-531.
45. H. A. Lorentz, *Proceedings of the Koninklijke Akademie Van Wetenschappen Te Amsterdam*, 1905, **7**, 684-691.
46. C. Wood, D. Emin, and P.E. Gray, *Phys. Rev. B,* 1985, **31**, 6811-6814.
47. J. L. Cohn, J. J. Neumeier, C.P. Popoviciu, K. J. McClellan and T. Leventouri, *Phys. Rev. B,* 1997, **56**, R8495-R8498.
48. Y. Zhang, N. P. Ong, Z. A. Xu, K. Krishana, R. Gagnon and L. Taillefer, *Phys. Rev. Lett.*, 2000, **84**, 2219-2222.
49. T. M. Tritt, *Thermal Conductivity: Theory, Properties, and Applications*, Kluwer Academic / Plenum Publishers, New York, 2004.

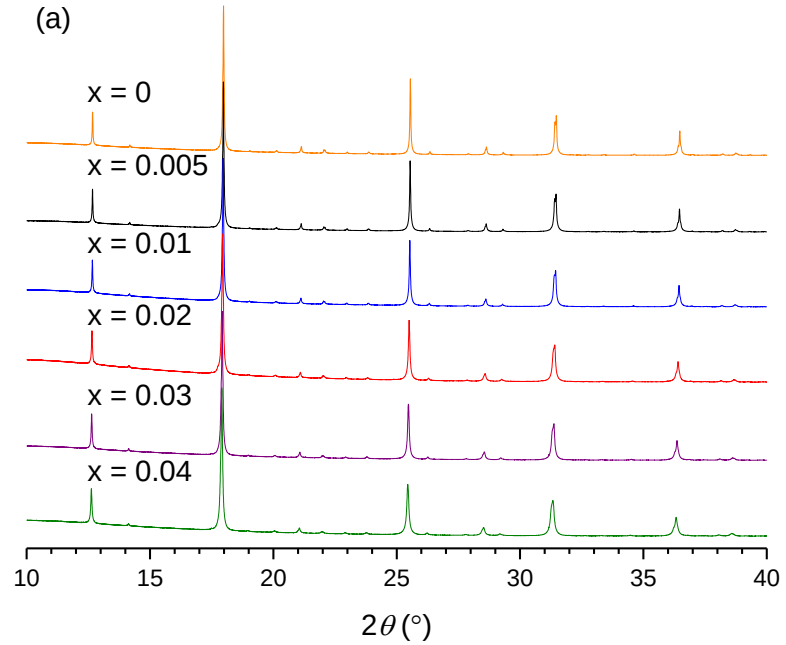
(a)
x = 0
x = 0.005
x = 0.01
x = 0.02
x = 0.03
x = 0.04
10
15
20
25
30
35
40
2θ (°)

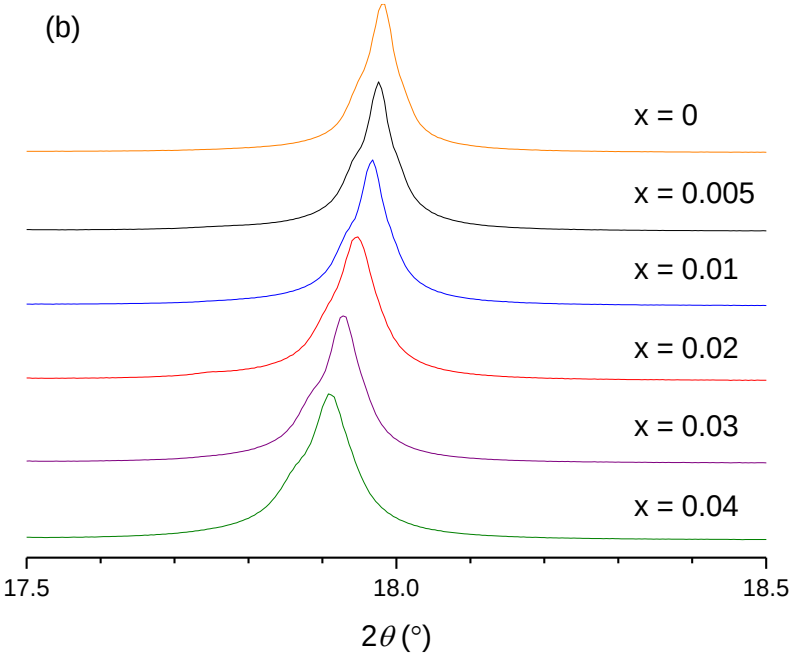
(b)
x = 0
x = 0.005
x = 0.01
x = 0.02
x = 0.03
x = 0.04
17.5
18.0
18.5
2θ (°)

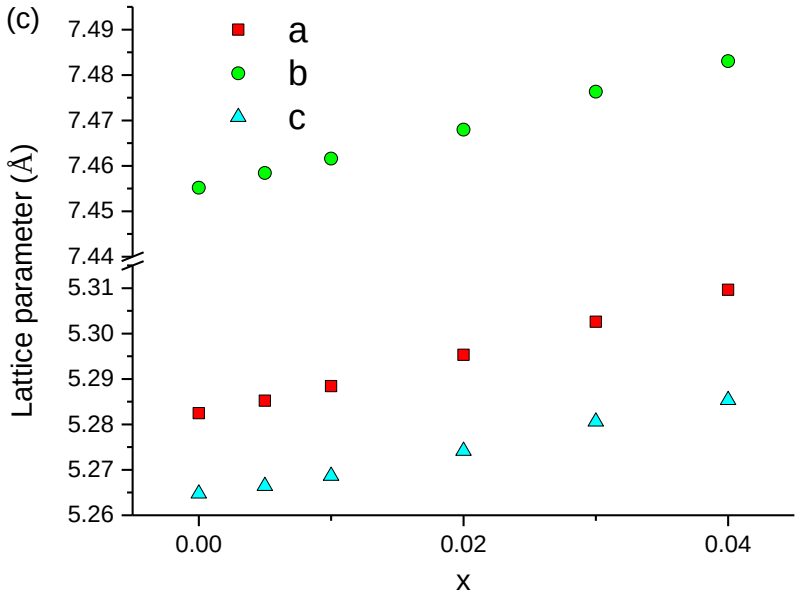

Figure 1 a) Synchrotron XRD patterns for the $CaMn_{1-x}Re_xO_3$ ($0 \leq x \leq 0.04$) series, b) the most intense Bragg reflections (*hkl* = 200, 121, 002) showing the steady shift towards lower angle with higher Re content and c) lattice parameters obtained by Pawley fitting with the *Pnma* space group. Errors are smaller than the symbol size. The Rietveld refinement details for x = 0.02 are presented in Supplementary Figure S5 and Table S2.

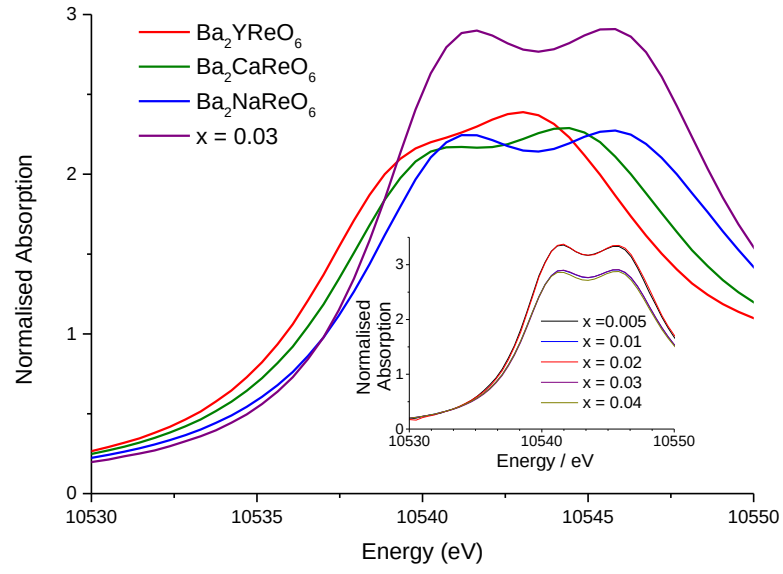

Figure 2 Normalised Re L_3-edge XANES spectra for the x = 0.03 and reference samples of known oxidation state of Re; $Ba_2YRe^{5+}O_6$, $Ba_2CaRe^{6+}O_6$ and $Ba_2NaRe^{7+}O_6$. Inset: Normalised Re L_3-edge XANES spectra for the $CaMn_{1-x}Re_xO_3$ ($0.05 \leq x \leq 0.04$) which show the identical edge positions for all the compositions.

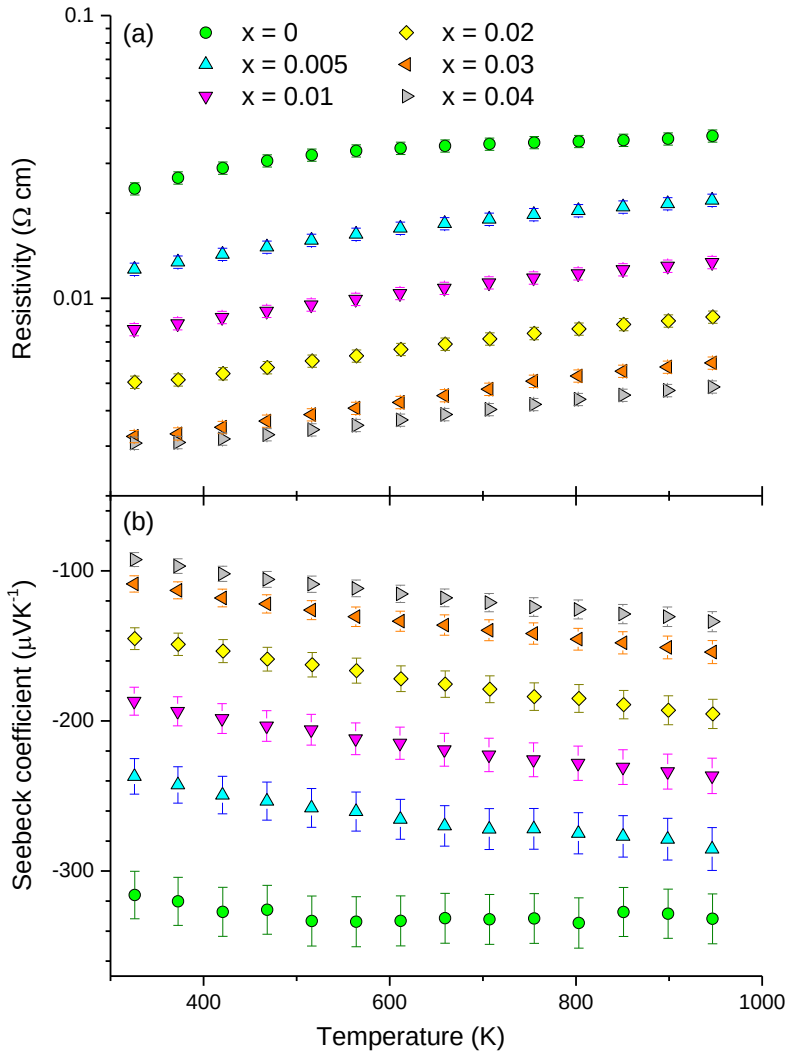

Figure 3 Plots of the a) resistivity and b) Seebeck coefficient between 326 K and 950 K for the $CaMn_{1-x}Re_xO_3$ ($0.00 \leq x \leq 0.04$).

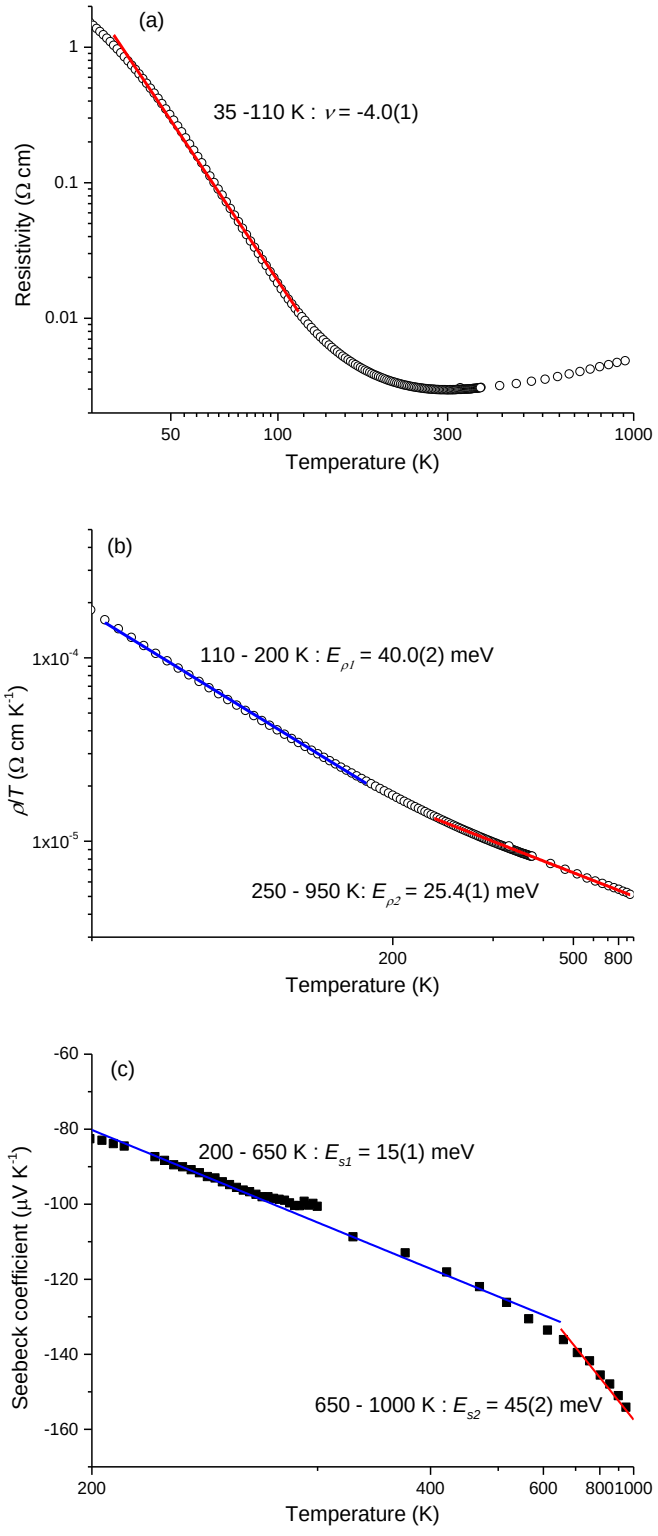

Figure 4 Temperature dependence of the electrical and thermoelectric properties of x = 0.03 from 35 K to 950 K. (a) log-log plot of the resistivity, the linear region presents a slope of -4.0(1) corresponding to the 3D Variable Range Hopping below 110 K. (b) Adiabatic small polaron analysis of the resistivity between 110 -950 K showing two activation energies (110 K – 200 K blue line with $E_{\rho 1}$=40.0(2) meV and 250 – 950 K red line with $E_{\rho 2}$=25.4(1) meV). (c) Activation energies

determination of the Seebeck coefficient between 200 - 950 K showing two linear regions: 200 K-650 K with E_{S1}=15(1) meV and 650 K- 100 K with E_{S2}=45(2) meV.

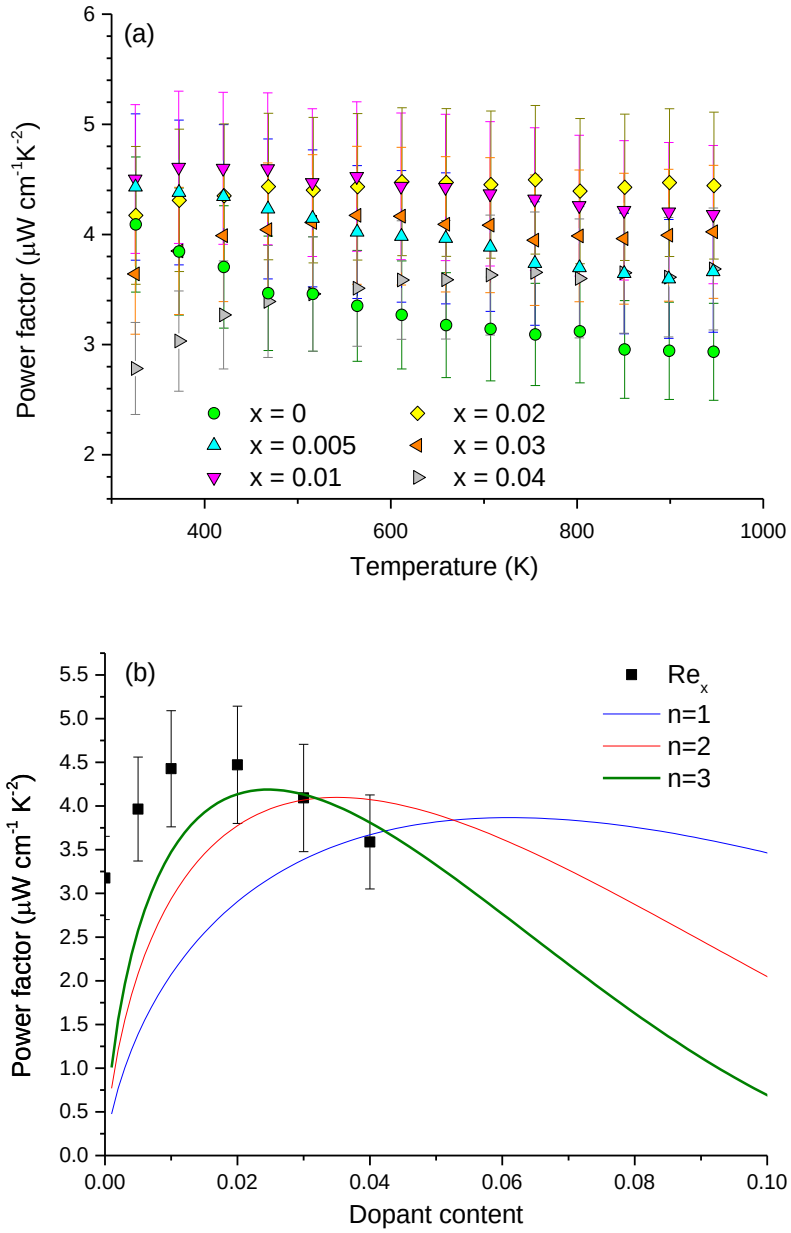

Figure 5 Power factor a) as a function of temperature and b) as a function of dopant content at 659 K for the $CaMn_{1-x}Re_xO_3$ ($0.00 \leq x \leq 0.04$). Solid lines in (b) are isothermal power factor calculated using the model described in the text for different oxidation state of a dopant element (n = 1 for pentavalent, 2 for hexavalent and 3 for heptavalent substitution).

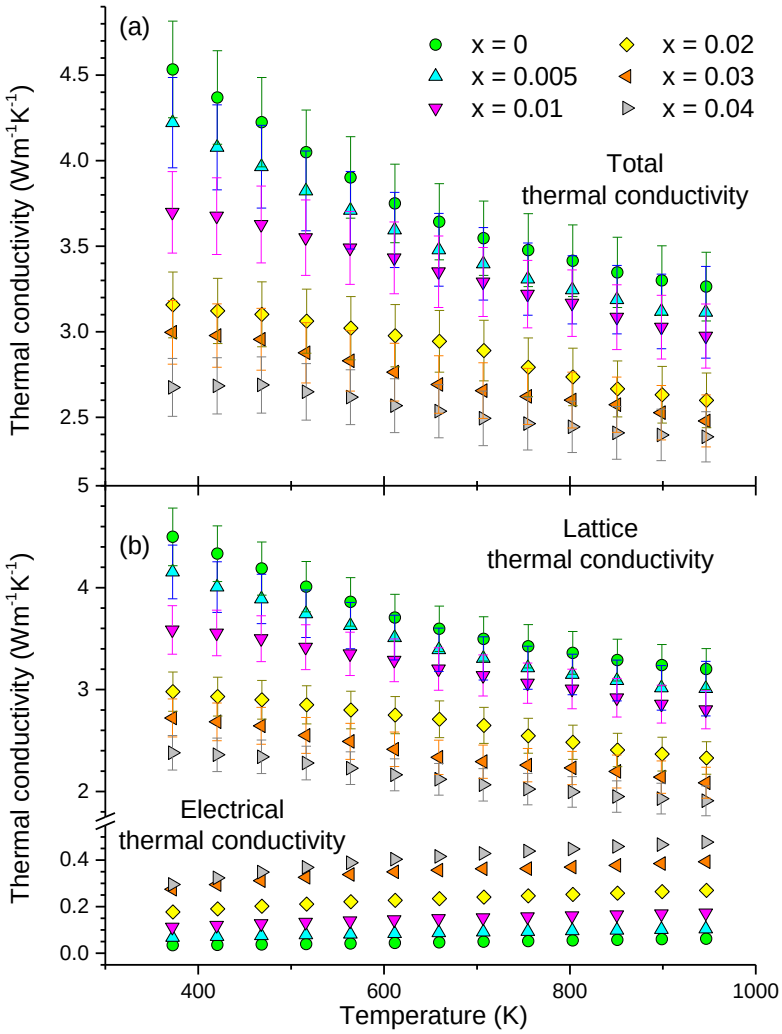

Figure 6 a) Total thermal conductivity and b) estimated lattice and electrical thermal conductivity as a function of temperature for the $CaMn_{1-x}Re_xO_3$ ($0.00 \leq x \leq 0.04$).

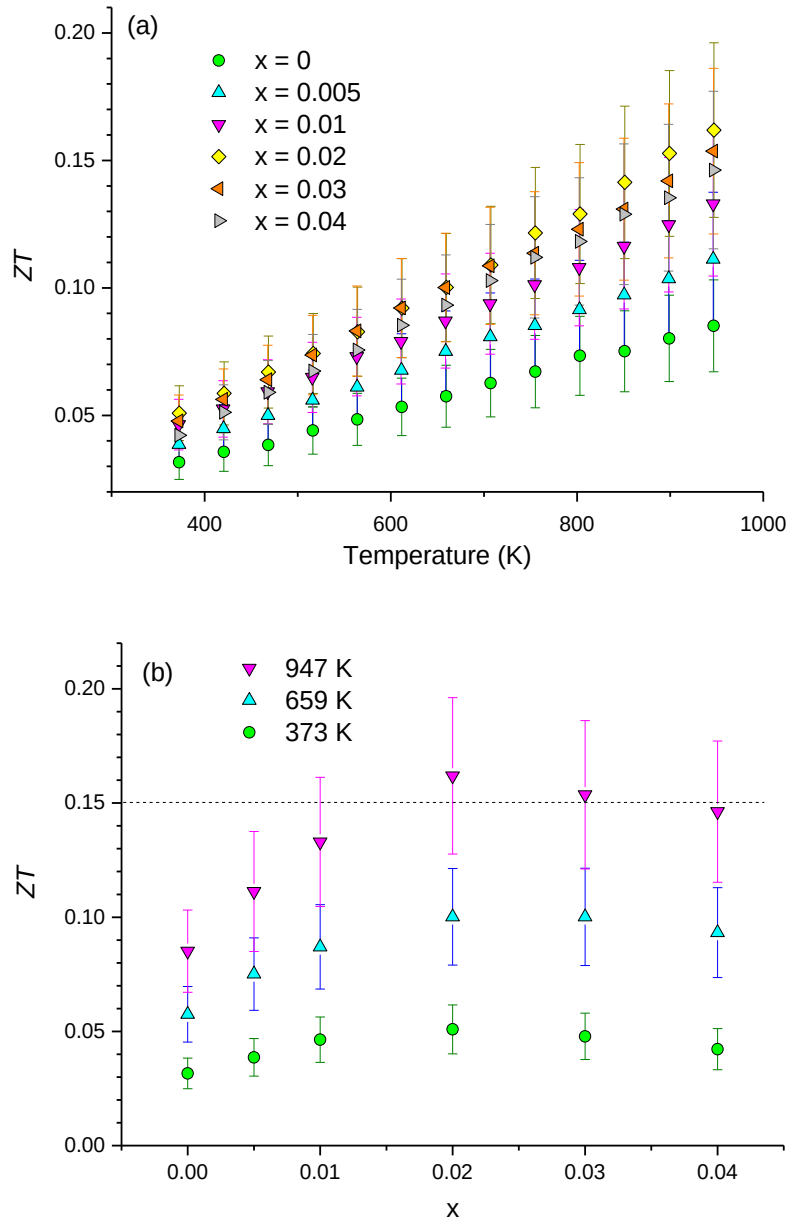

Figure 7 *ZT* for the $CaMn_{1-x}Re_xO_3$ ($0 \leq x \leq 0.04$) series as a function of a) temperature and b) Re content at 373, 659 and 947 K. Dotted lines in (b) is the highest *ZT* value (± 20%) for B-site doped $CaMnO_3$ at ≈ 950 K .[29]